Intensity-Modulated Spectroscopy on Loaded Organic Photovoltaic Cells

K. Adhitya, A. Alsulami, A. Buckley, Richard C. Tozer, Senior Member, IEEE, M. Grell

Abstract—We configured a generic digital lock-in amplifier as a light intensity-modulated spectrometer for photovoltaic (PV) cells for intensity-modulated spectroscopy (IMS) up to 250 kHz. We performed IMS on a state-of-the-art bulk heterojunction (BHJ) organic PV (OPV) cell and introduced a new mode of IMS wherein PV cells work under finite load, including maximum power point (MPP). Quantitative analysis supported by equivalent circuit simulations establishes MPP-IMS as favourable alternative to the commonly used intensity-modulated photovoltage/ photocurrent spectroscopy (IMVS/IMPS) modes. Using IMS under finite load, we identify a high frequency feature that is invisible in both IMPS and IMVS. The feature is ageing-related and becomes more prominent after long-term storage. We propose an extended equivalent circuit model that locates the origin of this feature at the BHJ itself, and link it to diffusion of indium ions etched from the transparent electrode by the hole extracting PEDOT:PSS. Finally, we introduce a method to determine BHJ capacitance by IMS without absolute calibration of light intensity.

Index Terms—Bulk heterojunction, intensity-modulated spectroscopy, maximum power point, organic photovoltaics, PEDOT:PSS.

I. Introduction

A. General

EMERGING photovoltaic (PV) cell technologies have to be operationally stable to transition from laboratory 'heroes' to commercially viable devices. In the case of bulk heterojunction (BHJ) organic photovoltaic (OPV) devices, stability is controlled by a number of internal and external factors: Internally, the electrochemical stability of the donor and acceptor materials and the chemical stability of the electrode materials are key. Externally, the ability of cost-efficient transparent encapsulation layers to prevent ingress of water and oxygen is essential. Also, excluding oxygen and water during manufacture is critical, which is emphatically demonstrated e.g. by the work of Luther et al. [1], wherein devices were purposefully exposed to oxygen during manufacture, with significant impact on their performance.

Common DC electrical characterisation under AM 1.5 illumination establishes a number of performance parameters, and their decay with operational lifetime. However, it can not fully discern the nature of degradation mechanisms in complex device architectures. For detailed understanding of a cell's internal processes, and clues towards degradation mechanisms, it is often helpful to study a solar cells' response to a dynamic (AC) stimulus.

B. Impedance- and Conventional Intensity Modulated-Spectroscopies (IMPS, IMVS)

Electrical impedance spectroscopy (EIS) is a widely established tool for the study of electrical networks and electrochemical systems under dynamic stimulus, and has been applied to assess dynamic processes, stability and degradation mechanisms in the different constituent layers of solar cells, e.g. by fitting measured impedance spectra to equivalent circuits, or drift/diffusion models [2-4]. However, since solar cells by design convert a light input into an electrical output, they are susceptible to an alternative, light-driven spectroscopy to study the dynamics of their internal processes, known as intensity-modulated spectroscopy (IMS). Typically, a fast LED is modulated to emit a light intensity $L + \Delta L\ sin\ \omega t$, $\Delta L < L$, that is projected onto a PV cell, and amplitude and phase of the cell's electrical response are recorded as a function of modulation frequency. IMS has been applied to various types of solar cells, including OPVs, dye-sensitised solar cells (DSSCs), and CdTe/CdS cells [1, 5-10]. Two modes of IMS are established in the literature, namely intensity- modulated photovoltage spectroscopy (IMPV) [8, 9], which records the frequency dependent modulation of a solar cell's open-circuit voltage (V_{OC}) under modulated L, and intensity-modulated photocurrent spectroscopy (IMPS) [1,5-7], recording the frequency dependent modulation of a solar cell's short-circuit current (I_{SC}). IMPS is more common, as for moderate or high L (including AM 1.5), V_{OC} is near-independent of L, while I_{SC} is proportional to L. Frequency dependency of the amplitude and phase of the PV cell's electrical response may be presented in Bode and/or Nyquist plots, like in EIS, albeit an IMS Nyquist plot does not display electric impedance. Instead, it may show real and imaginary part of ΔV (*Re ΔV / Im ΔV*, in Volts) for IMVS, or ΔI (in A) for IMPS when ΔL is not known in absolute terms, or of $\Delta V/\Delta L$ or $\Delta I/\Delta L$ (in Vm^2W^{-1}, or Am^2W^{-1}) when ΔL is known absolutely.

C. Intensity Modulated Spectroscopy Under Finite Load

Practically, solar cells operate neither under open circuit ('infinite' load resistor, R_L) nor short circuit (zero R_L) conditions, but under an electric load R_{MPP} with $0 < R_{MPP} < $ infinity that tunes the cell to its maximum power point voltage, V_{MPP}. Fig. 1 illustrates that IMS can be conducted on cells under a finite load, R_L:

K. Adhitya, A. Alsulami, A. Buckley and M. Grell are with The Department of Physics and Astronomy, The University of Sheffield, Hounsfield Road, Sheffield S3 7RH, UK (K. Adhitya e-mail : php08ka@sheffield.ac.uk).
 R. C. Tozer is with The Department of Electronic & Electrical Engineering, The University of Sheffield, Mappin Street, Sheffield S1 3JD, UK.

Fig. 1. (a) Schematic setup for IMS. R_L represents an external load. (b) DC Current/Voltage (I/V) characteristic of a PV cell under three different light intensities (L (blue); L - ΔL (green); and $L + \Delta L$ (red)). The load line for external load R_L is shown in black.

Schematic DC I/V characteristics of a given solar cell under different light intensities in the order AM 1.5 are illustrated in Fig. 1(b). I_{SC} increases in proportion to light intensity, V_{OC} is near constant. The load resistor R_L is represented by a load line. The intersection of the load line with the I/V characteristic gives the resulting DC voltage V of a solar cell illuminated by a particular light intensity, and loaded with R_L. We will call this V the 'voltage point' for R_L. Under light intensity modulation $\pm \Delta L$, V will be modulated by $\pm \Delta V$. In the limit of low frequency, ΔV can be read graphically by the intersections of the same load line with the I/V characteristics for $L \pm \Delta L$, as shown in Fig. 1(b). At higher modulation frequencies, the amplitude of ΔV will drop, and display a phase (φ) with respect to ΔL, leading to an IMS spectrum at R_L. Fig 1(b) reveals a weakness of both IMVS ($R_L \rightarrow$ infinity: Load line parallel to V axis) and IMPS ($R_L \rightarrow 0$: Load line parallel to I axis): In both cases the measured voltage modulation tends to zero even for low frequency, leading to difficulties in practical measurement. For IMPS, this has to be overcome by measuring current instead of voltage, using a current-to-voltage (I/V) converter. However, when R_L is chosen similar to R_{MPP}, we find a finite ΔV without I/V converter.

We here configure a generic digital lock-in as a bespoke IMS spectrometer, and introduce a new mode of IMS different from both the established IMVS and IMPS, by applying intensity-modulated light to OPV cells that are externally loaded with finite R_L, including R_{MPP}. We rationalise our results by comparison to simulations on a generic equivalent circuit model, and identify working near MPP as the optimum mode of IMS. We use IMS under finite load to study the ageing of stored OPV cells, and find an ageing-related high frequency feature that is invisible in both IMPS and IMVS. We can model the observed feature by extending the generic equivalent circuit at the BHJ capacitance branch. We link the ageing-related feature to prior reports on the chemical etching of ITO contacts by the acidic PSS dopant of the PEDOT:PSS hole extraction layer, and subsequent diffusion of indium ions [11, 12]. Finally, we establish a method to determine BHJ

capacitance by IMS without absolute calibration of LED intensity.

II. EXPERIMENTAL

A. Intensity-Modulated Spectroscopy Instrument

A commercial instrument for IMPS is available from Zahner [13], and impedance analysers can be adapted to work as IMPS instruments, e.g. [5]. Here, we have developed an alternative, far more affordable and portable intensity modulation instrument that can perform IMS at any point of a solar cell's I/V characteristic. We built our system (Fig. 2(a)) around the digital Anfatec USB 250 Lock-In amplifier [14], otherwise using only a PC with LabView software, and electronic small parts. Sinusoidal light intensity modulation is facilitated from the lock-in's reference voltage output. A bespoke voltage adder circuit, based on fast 2N2369 NPN transistors, is used to add a DC bias to the AC reference output. (Fig. 2b).

(a)

(b)

Fig. 2.(a) Block diagram of our IMS measurement setup, showing the PC running a LabView routine controlling the USB lock-in, a circuit driving a fast red LED by adding a DC offset voltage to the AC modulation voltage taken from the lock-in's reference output, the solar cell with its terminals connected via a variable load R_L, and the

voltage across the load fed into the lock-in's measurement input. (b) Circuit scheme of the DC + AC adder circuit, that adds a DC bias to the AC lock-in reference output to drive the LED. The lock-in reference output is represented by a voltage source, top left. DC voltage supply is from 2 x 9 V batteries stabilised by capacitors (right). The level of DC bias is set by a potentiometer. The LED (D1) is highlighted. As a performance test of the DC + AC adder, we fed the DC + AC signal directly into the lock-in measurement input, and found no measurable drop in AC amplitude, and less than 1° of added phase, up to 250 kHz.

Resulting DC + AC voltage is applied to a fast red LED (RC-LED, 650 nm) protected by a serial resistor of 120 Ω. The levels of DC voltage bias, and AC voltage modulation amplitude, are chosen so that the LED drive current is given by I_{LED} = (18 ± 4) mA. The resulting light intensity $L ± \Delta L$ is not known in absolute terms, but it is significantly smaller than AM 1.5. However, $L \sim I_{LED}$, hence $\Delta L/L = \Delta I/I$. A bespoke LabView routine sets the lock-in reference output frequency to values between 1 Hz and 250 kHz in 12 steps per decade, while the voltage drop $V + \Delta V(\omega) \sin(\omega t + \varphi(\omega))$ across R_L is fed into the lock-in voltage measurement input, without pre-amplifier or current-to-voltage converter. Amplitude and phase of voltage modulation ΔV are recorded as function of $f = \omega/2\pi$. Additionally, we ran IMS measurements with a variety of added external load capacitors C_L in the order 1-nF parallel to R_L, cf. table I. The LED drive current modulation was reduced to ±1 mA with unchanged 18 mA DC bias. Rather than recording full IM spectra, we manually tuned modulation frequency until phase equalled -45°; this frequency is known as 'corner frequency', f_c. We also recorded modulation amplitude at -45° and compared to modulation amplitude in the low frequency limit.

B. Organic Solar Cell Preparation and Characterisation

We here studied a state-of-the-art BHJ OPV cell using as its active layer a blend of a low bandgap hole transporting semiconducting polymer, abbreviated PFDT2BT-8 (inset to Fig. S1, supplementary information), and an electron accepting C_{70} derivative, with a PEDOT:PSS hole extracting layer. The synthesis of PFDT2BT-8 is described in [15]. Active device area was 2.86 mm^2, small enough to be illuminated entirely by the bright spot of our LED. Details of cell manufacture, characterisation, and selection of suitable cells are described in our supplementary information. In brief, the performance characteristics of OPV 'pixel' used here were j_{SC} = -10.7 mAcm^{-2}, V_{OC} = 902 mV, maximum power point at V_{MPP} = 680 mV, and maximum power density P_{MPP} 6.2 mWcm^{-2}, shunt resistance R_{Sh} = 70 kΩ, and serial resistance R_S = 520 Ω under AM 1.5 illumination. However, performance parameters were significantly different under the much less intense illumination by our red LED driven at 18 mA, namely j_{SC} = -0.51 mAcm^{-2}, V_{OC} = 800 mV, V_{MPP} = 650 mV, and P_{MPP} = 270 μWcm^{-2}, R_{sh} = 350 kΩ and R_s = 6.4 kΩ. For the simulation of impedance spectra of loaded OPV cells by

equivalent circuit models, we used LT SPICE software version IV from Linear Technology [17]. We customised the properties of rectifying diodes used in equivalent circuits, in particular we selected a much reduced saturation (reverse bias) current, in the order pA rather than nA as found in stock (inorganic) diodes.

III. RESULTS AND DISCUSSION

A. Intensity-Modulated Spectra Taken Under Finite Load

Fig. 3(a) shows the family of measured IMS spectra as Nyquist plots when R_L is set to a range of different values, giving load lines with different slope, hence different voltage points. Variation of R_L sweeps out the DC I/V characteristic from voltage point V close to 0 (short circuit, R_L near zero), to V close to V_{OC} ($R_L \rightarrow$ infinity). Fig. 3(b) shows 3 of the curves from 3(a) (near open circuit, near short circuit, near MPP) on a normalised scale to compare their shape.
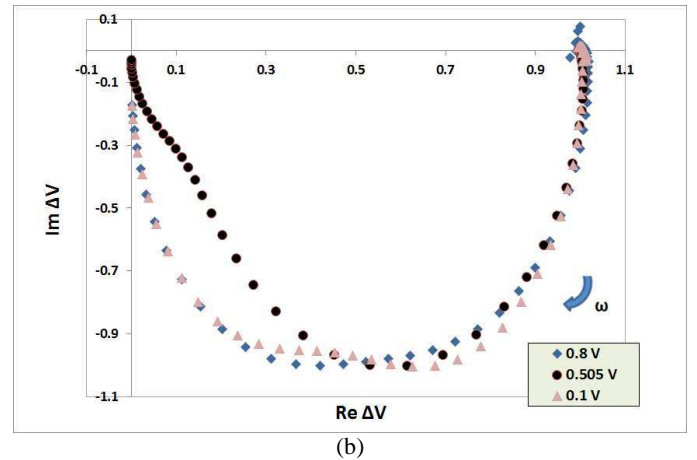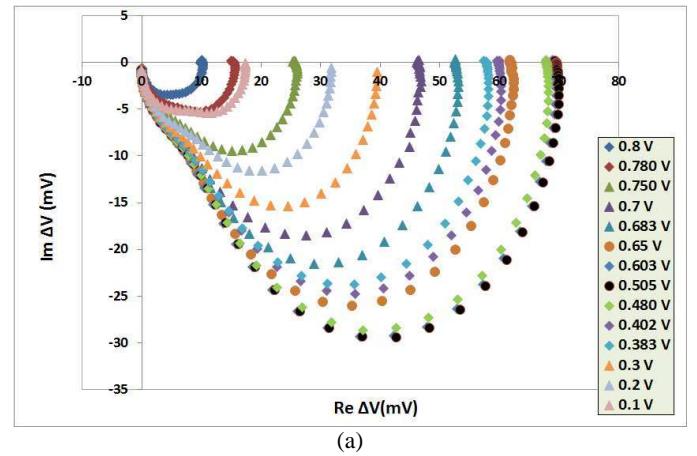

(a)

(b)

Fig. 3. (a) Nyquist plots imaginary part of ΔV (I$m \Delta V = |\Delta V| \sin\varphi$) vs. real part of ΔV (Re $\Delta V = |\Delta V| \cos\varphi$), parametric in frequency for IMS spectra taken at different R_L, ranging from near-open circuit (high R_L, 'IMVS') to near-short circuit (low R_L, 'IMPS'). Spectra are labelled

by their voltage points, V, shown in the panel on the right, rather than R_L. LED was driven by (18 ± 4) mA. Note Re / Im axis use different scales. (b) Normalised Nyquist plots of Fig. 4a taken at near-open circuit voltage point (0.8 V, R_L = 476 kΩ), near maximum power point (0.505 V, R_L = 36.6 kΩ) and near-short circuit voltage point (0.1 V, R_L = 6.8 kΩ). Direction of increasing frequency is given by the blue arrow. In all plots, *Re ΔV* is normalized to its value in the limit of f $\to$ 0 Hz, whilst *Im ΔV* is normalized to its minimum magnitude.

For all settings of R_L, the general shape of our IMS Nyquist plots is dominated by a semicircle (or, semi-ellipse- note the scales on Re / Im axis differ) in the 4th quadrant of the complex plane. However, the characteristic parameters of the semicircles change with R_L, and there is a 'shoulder' feature at high frequencies that deviates from perfect semicircular shape for most choices of load resistance R_L. However, Fig. 3(b) shows this 'shoulder' is largely absent in the extreme cases, high R_L (approaching open circuit, IMVS mode) and low R_L (approaching short circuit, IMPS mode). IMPS and IMVS spectra are somewhat flattened compared to a perfect semicircle, but without the distinct 'shoulder' feature seen at MPP load, which would therefore be missed in the traditional IMVS and IMPS modes. We first investigate and rationalise the dependency of the dominant semicircles' characteristics with R_L, using a generic equivalent circuit model (inset Fig. 5) that describes the dominant semicircle's parameters. Then, we discuss the origin of the high frequency shoulder in the context of previous work.

B. Magnitude and Corner Frequencies: Measurement vs. Generic Equivalent Circuit Modelling

The characteristic parameters of our Nyquist semicircles are their magnitude, characterised by the limit of *Re ΔV* (f $\to$ 0), and the 'corner frequency', f_c, which is given by the frequency where *Im ΔV* has its minimum (i.e., maximum magnitude). *Re ΔV* (f $\to$ 0) is equal to the DC ΔV shown in Fig. 1(b). The electric conditions (loads R_L and DC voltage points, i.e. the voltages selected by the respective R_L, as well as the corresponding current densities j under LED illumination), and characteristic parameters f_c, *Re ΔV (f $\to$ 0))* of the IMS spectra shown in Fig. 3 are summarised in table S1 (supplementary information), and plotted in Fig. 4.
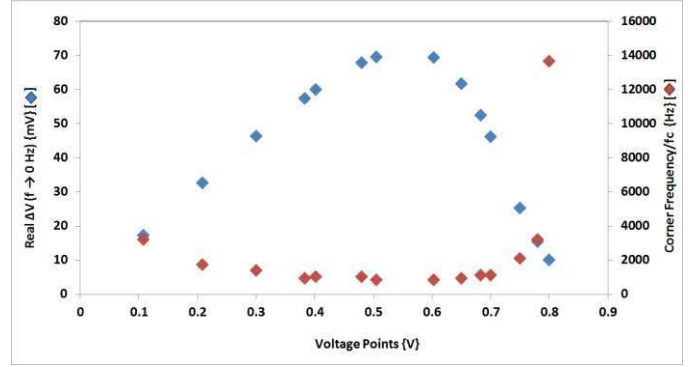

Fig. 4. The characteristic parameters of the dominant Nyquist semicircle plotted against voltage point, which is set by R_L. Blue: Re ΔV at low frequency (f $\to$ 0) vs. voltage points. Red: Corner frequencies, f_c, vs. voltage points.

The small amplitudes of *Re ΔV* (f $\to$ 0) for both small, and large, values of R_L (i.e. voltage point approaching 0 and V_{OC}, respectively) are easily understood as low/high R_L corresponds to a near-vertical, or near-horizontal, load line in Fig. 1(b), leading to small ΔV. The *Re ΔV* (f $\to$ 0) profile for intermediate loads, is similar in shape to the power profile in Fig.s S1 and S4 (supplementary information). *Re ΔV* (f $\to$ 0) peaks at voltage point V_{MAX} = 550 mV, somewhat below V_{MPP} = 650 mV from the power profile under LED illumination (Fig. S4). Corner frequencies are high for both, voltage points approaching short circuit, and voltage points approaching V_{OC}, with a broad minimum around MPP.

To rationalise our results we compared to LT SPICE simulations on a generic OPV equivalent circuit (e.g. Narayan) that was loaded externally by R_L, see inset to Fig. 5. As circuit components representing our OPV cells, we selected R_{Sh} = 100 kΩ, R_S = 2 kΩ << R_{Sh}, (Similar to the parameters extracted from Fig.s S1 and S4, supplementary information); C_{BHJ} = 4 nF (for magnitude of C_{BHJ}, cf. section D), and a modified 1N914 diode designated as 1N914_KA. Diode modification consisted of selecting a lower reverse bias saturation current (I_S). I_S influences the equivalent circuit's V_{OC}, and I_S = 3 pA was chosen so that the equivalent circuit replicates the observed V_{OC} of our OPV cell. The magnitude of the current source was set to 25 μA DC with an AC modulation of 5 μA. Fig. 5 shows a simulated 'Nyquist rainbow' under different R_L in the order kΩ ($R_S < R_L < R_{Sh}$), corresponding to experimental results in Fig. 3.
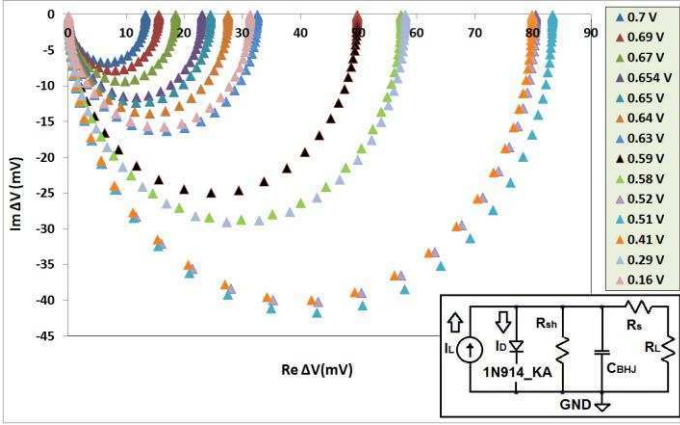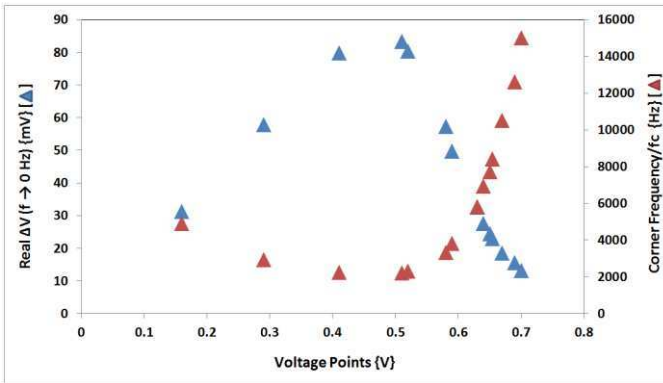
Fig. 5. Simulated 'Nyquist rainbow' for the generic OPV equivalent circuit model, shown as inset. I_L represents the light- driven current source. In IMS, all components apart from R_L are internal to the OPV cell. We selected R_{Sh} = 100 kΩ, R_S = 2 kΩ, C_{BHJ} = 4 nF, and a customised 1N914 diode (1N914_KA) with the saturation current reduced to 3 pA. The amplitude of current source modulation was set to 5 μA and the DC current bias was set to 25 μA. R_L was varied in the range (6.8-476) kΩ, leading to the voltage points shown in the panel on the right. The largest semicircle (light blue symbols) corresponds to R_L = 26.5 kΩ.

Simulated Nyquist plots of the generic OPV equivalent circuit give exact semicircles/ellipses at all voltage points without the observed high frequency 'shoulder' even when simulated cells are loaded to near MPP, but semicircles show different magnitude $Re\ \Delta V$ (f → 0), and corner frequency f_c for different voltage points. For comparison to experimental results, we plot characteristic features of the simulated equivalent circuit in Fig. 6, which corresponds to Fig. 4.

Fig. 6. The characteristic parameters of the simulated Nyquist semicircle plotted against voltage point V, which is set by R_L. (a) Re ΔV at low frequency (f → 0) vs. voltage points. (b) Corner frequencies, f_c, vs. voltage points. $Re\ \Delta V$ reaches its maximum for R_L = 26.5 kΩ.

For both experimental and simulated spectra, the magnitude of $Re\ \Delta V$ (f → 0) strongly depends on the magnitude of R_L, i.e. voltage point, V. The $Re\ \Delta V$ (f → 0) vs. voltage point plots for

experiment (Fig. 4) and simulation (Fig. 6) are very similar, both resembling a power profile, peaking near MPP. The broad and flat minimum of f_c shown in Fig. 4 is also replicated by simulation, Fig. 6. Quantitatively, f_c is about 3 times higher in simulation than in experiment. Quantitative differences for f_c probably mainly arise from the difficulties of simulating the nonlinear properties of an organic BHJ diode in the equivalent circuit model with conventional software. Note Gundlach et al. [6] have avoided the diode in their simulations altogether, linearising it by an incremental resistor. This is acceptable when a single, fixed voltage point is studied (indeed we do this ourselves in section D), but not when we study voltage point dependency of f_c, as the diode incremental resistance does change (non- linearly) with voltage point. The SPICE software offers a selection of stock inorganic diodes, with the option for customising. To account for two of the differences between stock diodes and organic BHJ diodes, we selected a significantly smaller saturation current (order pA vs. nA) due to lower carrier mobility, and added 4nF C_{BHJ} // diode to add to the (order pF) capacitance of a stock diode, albeit C_{BHJ} is not voltage- dependent, while diode capacitance is [4]. We also do not know the ideality factor (n) of our BHJ OPV diode, or if it is quantitatively described by the standard diode equation at all. The observed behaviour of $Re\ \Delta V$ (f → 0) (a DC property) under different R_L can therefore be understood near- quantitatively by the generic equivalent circuit model, inset to Fig. 5, but f_c (AC property) only qualitatively. Practically, the increased modulation amplitude ΔV, and reduced corner frequency, under loads near R_{MPP} are welcome: Increased amplitude improves signal-to-noise ratio, and reduced corner frequency effectively extends the instrumental bandwidth to higher frequencies. The latter can be seen in Fig. 3(b), where the MPP spectrum approaches the origin more closely than either IMPS or IMVS spectra, although all terminate at the same frequency, 250 kHz. We thus propose a new mode of IMS working at MPP, rather than the established open circuit (IMVS)- and short circuit (IMPS) modes, as both the most realistic and practically most convenient mode of IMS.

C. Spectral Features at High Frequency: Relation to Cell Ageing

At high frequencies, there remains a difference between experiment and generic circuit simulation results, namely a high frequency 'shoulder' in experimental spectra taken under finite loads, in particular when $R_L \sim R_{MPP}$. This feature is invisible near open circuit (IMVS mode) and near short circuit (IMPS mode), cf. Fig. 3(b). Qualitatively, in IMPS, most current generated by the cell's current source will flow through the external short circuit. Under open-circuit conditions, the cell's internal diode will be strongly forward-biased, resulting in a low resistance internal current path. Under finite load, however, both external current path, and internal diode, display significant resistance, thus forcing more current through the BHJ capacitance path, in particular at high

frequencies, when capacitive impedance drops. Thus IMS under finite load may reveal latent spectral features originating at the BHJ that remain hidden in IMPS and IMVS modes. For comparison, Semenekhin et al [9] previously reported IMPS and IMVS on a similar OPV cell but using a different light absorbing / hole conducting polymer in the BHJ blend. They observed a marked difference between IMPS and IMVS spectra, which we find to be rather similar (cf. Fig. 3(b)), but like here, neither their IMPS nor IMVS spectra display a high frequency 'shoulder'. Instead Semenekhin et al report a strong '3rd quadrant' (negative $Re\ \Delta V$) high frequency feature in IMPS that is absent in IMVS [9]. Negative $Re\ \Delta V$ is associated with the finite transit time of carriers between exciton splitting at the heterojunction and extraction at the contacts [9]. Here, spectra under all loads, including near-IMPS, remain in the 4th quadrant, suggesting faster carrier extraction.

We find the high frequency 'shoulder' seen under finite load is exacerbated by aging of OPV cells. We repeated IMS on a cell after it was stored in dark conditions under ambient atmosphere for 30 days. An AM 1.5 characterisation of a stored cell (not shown here) shows that j_{SC} has dropped to 3.2 mA/cm^2, V_{OC} and V_{MPP} dropped to 879 and 620 mV, respectively, and the maximum power to 1.6 mW/cm^2, with corresponding increase of R_{MPP} compared to a fresh cell. R_{Sh} and R_S under AM 1.5 have increased to 2.4 kΩ and 120 Ω, respectively. Fig. 7 compares Nyquist plots of IMS spectra at same R_L (61 kΩ) before and after storage.

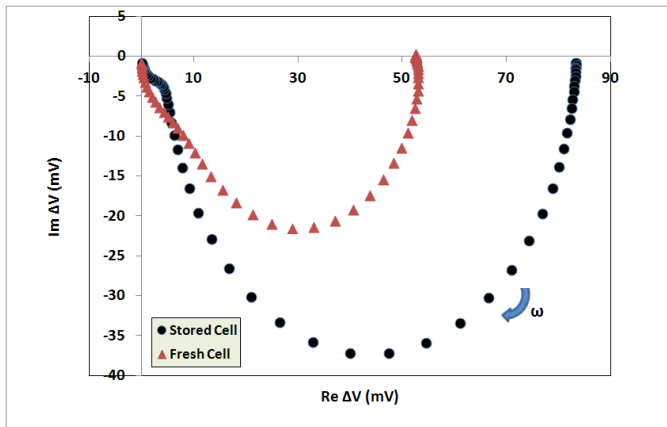Fig. 7. Comparison between the IMS spectra of a freshly prepared sample, and a sample stored 30 days under air in the dark. R_L = 61 kΩ for both. The corner frequencies (f_c) of the fresh and stored sample are 1140 Hz and 356 Hz respectively.

The overall larger size of the Nyquist plot indicates that R_L = 61 kΩ leads to a voltage point close to the peak of the $Re\ \Delta V$ (f → 0) vs. voltage point profile for the degraded cell, but not for the fresh cell, where the corresponding voltage point of 683 mV is in the steeply declining flank of the profile (cf. Fig. 4). However, the high frequency feature for the aged cell is now more clearly separated from the dominant semicircle, morphing from 'shoulder' to 'foot'.

Prior qualitative reasoning suggests that the high frequency feature seen for loaded cells originates at the BHJ. We therefore extended the generic equivalent circuit by a resistor parallel to a capacitor (R // C) in series with the BHJ capacitance. Fig. 8 shows the extended equivalent circuit, and simulated spectra for different magnitudes of the added R_{ext} // C_{ext}.
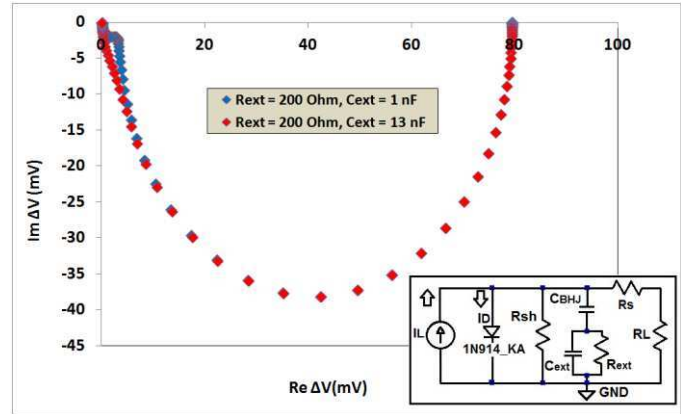

Fig. 8. Simulations on extended equivalent circuit model, shown as inset. R_L was set to 61 kΩ; R_{Sh}, R_S, C_{BHJ} were chosen to match the measured values for the stored cell under AM 1.5. (See below for measurement of C_{BHJ}). For simplicity, the diode was represented by a suitable (5.5 kΩ) incremental resistor (see below; similar as in Gundlach et al [6]). Red symbols: C_{ext} = 13 nF // R_{ext} = 200 Ω; blue symbols: C_{ext} = 1 nF // R_{ext} = 200 Ω.

When suitable parameters for R_{ext} // C_{ext} are chosen, simulated spectra now include the high frequency 'shoulder' or 'foot' features, similar as in experimental spectra (Fig. 7). The weaker high frequency feature for a 'fresh' sample captures aging at an early stage; note that a larger value of C_{ext} results in a smaller modification of C_{BHJ}. Modelling thus confirms the origin of the ageing-related high frequency feature is located at the BHJ itself.

OPV aging was the subject of detailed recent studies [18, 19], who reported a number of different degradation mechanisms. An important mechanism that will occur even in dark storage is the etching of ITO electrodes by the acidic dopant of the PEDOT:PSS hole extraction layer, polystyrene sulfonic acid (PSS), which liberates indium ions. A Rutherford Backscattering Spectrometry (RBS) study by Janssen et al [11], and TOF-SIMS studied by Jonkheijm et al [12], on model devices with PEDOT:PSS hole extracting layer showed that Indium will subsequently diffuse across the hole extracting layer into the BHJ region. We therefore assign the ageing-related high frequency feature to the diffusion of indium ions that originate from the etching of ITO by PSS to the BHJ.

D. Measuring Bulk Heterojunction Capacitance

Finally, we used IMS on a stored sample to determine the BHJ capacitance, in the sense of C_{BHJ} within the equivalent circuit model (inset to Fig. 5), at a voltage point near MPP. C_{BHJ} is not accessible from DC j/V measurements. Instead, we added different external capacitive loads, C_L, in parallel to fixed external $R_L = 32.7$ kΩ (C_L // R_L), and identified f_c as described in 'experimental'. Corner frequencies dropped with increasing parallel C_L, as shown in Table I.

TABLE I
CORNER FREQUENCY VS. EXTERNAL LOAD
CAPACITANCE, C_L. R_L WAS FIXED AT 32.7 kΩ

C_L [nF]	f_c [kHz]
0	2.4
0.39	2.16
0.47	2.14
1	1.91
2.2	1.59
4.7	1.09

To evaluate the behaviour of IMS spectra under C_L // R_L, we (mentally) replace the diode in the generic equivalent circuit, inset Fig. 5, by its incremental resistor R_D, which is justified for a given voltage point and small modulation amplitudes ($\Delta L \ll L$; note we dropped ΔI to 1 mA to find f_c under C_L). With R_D replacing the diode in the circuit inset Fig. 5, its corner frequency is given by eq. (1):

$$1/\omega_C = 1/(2\pi f_C) = C_{BHJ}\left(R_D \, // \, R_{Sh} \, // \, R_L\right) \qquad (1)$$

Wherein the '//' symbol stands for the total resistance resulting from parallel resistors. When an external load capacitor C_L is added parallel to load R_L, the extended circuit (indicated by prime in eq. (2)) is characterised by corner frequency:

$$1/\omega_C' = 1/(2\pi f_C') = \left(C_{BHJ} + C_L\right)\left(R_D \, // \, R_{Sh} \, // \, R_L\right) \qquad (2)$$

Eq.s (1),(2) rely in two assumptions, namely, that $R_S \ll R_L$ and hence R_S can be neglected in the expression for the total effective resistance, (R_D // R_{SH} // ($R_L + R_S$)), seen by the photocurrent source, I_L; and $R_S C_L \ll (C_L + C_{BHJ})$ (R_{Sh} // R_D). We verified the latter by checking that the two criteria for f_c (-45° phase shift, -3 dB amplitude drop = drop to 71% w.r.t. low frequency modulation amplitude) are met simultaneously. This observation also implies that the pole resulting from C_{BHJ} is well separated from any higher frequency pole due to C_{ext} (as defined in inset to Fig. 8). This agrees with the earlier observation that high frequency 'shoulder' features in Nyquist plots are clearly separated from the dominant, lower frequency corner due to C_{BHJ}. High frequency features related to C_{ext} thus

do not interfere with our determination of C_{BHJ}; on the other hand, we can not determine the magnitude of C_{ext} in the way described here.

Division of equations (1)/(2) leads to Eq.s (3a),(3b), which are mathematically equivalent:

$$C_{BHJ} = C_L\left(f_C'/(f_C - f_C')\right) \qquad (3a)$$

$$f_C / f_C' = C_L/C_{BHJ} + 1 \qquad (3b)$$

Eq. (3a) relates the unknown BHJ capacitance to known C_L, and measured corner frequencies, without knowledge of ΔL in absolute terms, nor of resistors R_D, R_S, R_{Sh}. Eq. (3b) suggests a plot of f_c / f_c' vs C_L, giving a straight line that intercepts the C_L axis at -C_{BHJ}, thus allowing determination of C_{BHJ} by extrapolation. Fig. 9 shows a plot of the data from Table I in the form suggested by eq. (3b).

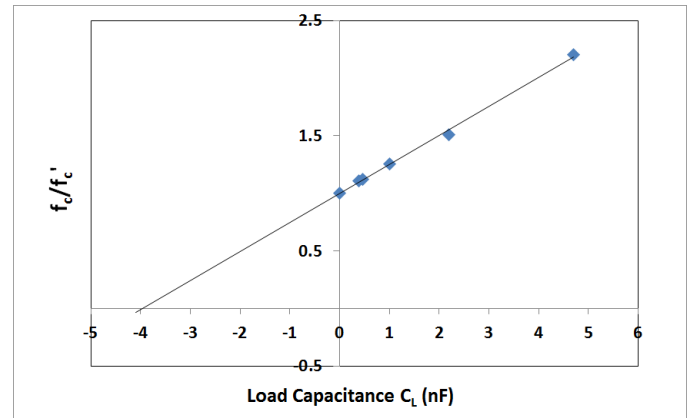Fig. 9. Ratio of corner frequencies for OPV cells not capacitively loaded / loaded with C_L // $R_L = 32.7$ kΩ vs. magnitude of capacitive load, C_L. Data from Table I. The straight line fit intercepts the C_L axis at - 3.9 ± 0.1 nF.

We find a very good straight line fit which indicates the underlying assumptions are met.–We therefore extrapolate a BHJ capacitance of 3.9 nF, corresponding to a specific capacitance of approximately 140 nF/cm². For comparison, we estimate a hypothetical 'geometric' specific capacitance, by 'modelling' a BHJ OPV as a parallel plate capacitor of thickness d = 100 nm separated by a dielectric medium of dielectric constant k = 1.5. This gives $C_{GEO} = 13.3$ nF/cm², an order of magnitude smaller than the actual BHJ capacitance. This discrepancy clearly illustrates the inadequacy of approximating a BHJ by a parallel plate capacitor, as this ignores the BHJ's large internal interface area. Since maximising internal interface area is the objective of BHJs, we propose the BHJ specific capacitance as an indicator of BHJ quality.

IV. CONCLUSION

We report a combined experimental and theoretical study of light intensity-modulated solar cell spectroscopy (IMS) on bulk heterojunction (BHJ) organic photovoltaic (OPV) cells. We designed and built a cost-effective IMS spectrometer from generic lab equipment, and introduce a generalised mode of IMS by loading PV cells with resistors, R_L. The previously established 'Intensity-modulated photocurrent spectroscopy' (IMPS) ($R_L \rightarrow 0$) and 'intensity-modulated photovoltage spectroscopy' (IMVS) ($R_L \rightarrow$ infinity) are the extreme cases of the more general mode introduced here. We rationalise the observed IMS spectra under different loads by simulations on a generic equivalent circuit model. Loading cells to maximum power point (MPP) emerges as the optimum mode of IMS: MPP is the realistic working condition for a solar cell, measured signal (and hence, signal-to-noise ratio) is largest for given modulation amplitude, and corner frequency is lowest, thus effectively extending IMS to higher frequency. Also, we observe an ageing-related high frequency feature in the IMS spectra of loaded cells that are invisible in both IMPS and IMVS. These can be accounted for by introducing a modification on the BHJ capacitance branch of the generic circuit model, thus locating the cause of the ageing-related feature at the BHJ itself. Finally, we introduce an experimental procedure and data analysis scheme to determine BHJ capacitance by IMS without detailed knowledge of equivalent circuit parameters, and without absolute calibration of light intensity modulation amplitude.

REFERENCES

[1] Y. T. Set , M. D. Heinemann, E. Birgersson, and J. Luther, "On The Origin of Quadrant I Semicircle in Intensity-Modulated Photocurrent Spectra of P3HT:PCBM Bulk Heterojunction Solar Cells: Evidence of Degradation-Related Trap-Assisted Recombination," J. Phys. Chem. C, vol. 117, pp. 7993-8000, 2013.

[2] G. Perrier, R. de Bettignies, S. Berson, N. Lemaitre, and S. Guillerez, "Impedance Spectrometry of Optimized Standard and Inverted P3HT-PCBM Organic Solar Cells," 2012, pp. 210-216.

[3] X. Chen, D. Taguchi, T. Shino, T. Manaka, and M. Iwamoto, "Analysis of interface carrier accumulation and relaxation in pentacene/C_{60} double-layer organic solar cell by impedance spectroscopy and electric-field-induced optical second harmonic generation," J. Appl. Phys., vol. 110, 2011.

[4] G. Garcia-Belmonte, A. Munar, E. M. Barea, J. Bisquert, I. Ugarte, and R. Pacios, "Charge carrier mobility and lifetime of organic bulk heterojunctions analyzed by impedance spectroscopy," Organic Electronics, vol. 9, no. 5, pp. 847-851, Oct, 2008.

[5] N. Kavasoglu, A. S. Kavasoglu, O. Birgi, and S. Oktik, "Intensity modulated short circuit current spectroscopy for solar cells," Solar Energy Materials & Solar Cells, vol. 116, pp. 727-730, 2011.

[6] B. H. Hamadani, J. Roller, P. Kounavis, N. B. Zhitenev, and D. J. Gundlach, "Modulated photocurrent spectroscopy of CdTe/CdS solar cells-equivalent circuit analysis," Solar Energy Materials & Solar cells, vol. 116, pp. 126-134, 2013.

[7] M. Bag, and K. Narayan, "Universality in Intensity Modulated Photocurrent in Bulk-Heterojunction Polymer Solar Cells," Phys. Rev. B, vol. 82, pp. 1-4, 2010.

[8] J. Krueger, R. Plass, M. Graetzel, P. J. Cameron, and L. M. Peter, "Charge transport and back reaction in solid-state dye-sensitized solar cells: a study using intensity-modulated photovoltage and photocurrent spectroscopy," Journal of Physical Chemistry B, vol. 107, pp. 7536-7539, 2003.

[9] J. C. Byers, S. Ballantyne, K. Rodionov, A. Mann, and O. A. Semenikhin, "Mechanism of recombination losses in bulk heterojunction P3HT:PCBM solar cells studied using intensity modulated photocurrent spectroscopy," Applied Materials and Interfaces 3, vol. 3, pp. 392-401, 2011.

[10] P. M. DiCarmine, and O. A. Semenikhin, "Intensity modulated photocurrent spectroscopy (IMPS) of solid-state polybithiophene-based solar cells," Electrochimica Acta, vol. 53, pp. 3744-3754, 2008.

[11] J. K. J. van Duren, J. Loos, F. Morrissey, C. M. Leewis, K. P. H. Kivits, L. J. van Ijzendoorn, M. T. Rispens, J. C. Hummelen, and R. A. J. Janssen, "In-situ compositional and structural analysis of plastic solar cells," Advanced Functional Materials, vol. 12, pp. 665-669, 2002.

[12] C. W. T. Bulle-Lieuwma, W. J. H. van Gennip, J. K. J. van Duren, P. Jonkheijm, R. A. J. Janssen, and J. W. Niemantsverdriet, "Characterization of polymer solar cells by TOF-SIMS depth profiling," Applied Surface Science, vol. 203, pp. 547-550, 2003.

[13] C. K. Zahner-elektrik, "Zahner Highend Data Acquisition Systems; CIMPS," 2015, p. http://www.qrins.com/ckseo/za/ctlg/cimps.pdf.

[14] A. Anfatec Instruments, "USB LOCKIN 250 LOCKIN AMPLIFIER AMPLIFIER 10 mHz to 250 kHz," 2015, p. http://www.anfatec.net/downloads/USBLockIn/USBLockIn250_Manual.pdf.

[15] D. C. Watters, H. Yi, A. J. Pearson, J. Kingsley, A. Iraqi, and D. Lidzey, "Fluorene-Based Co-polymer with High Hole Mobility and Device Performance in Bulk

Heterojunction Organic Solar Cells," Macromolecular Rapid Communications, vol. 34, pp. 1157-1162, 2013.

[16] D. T. Cotfas, P. A. Cotfas, and S. A. Kaplanis, "Methods to Determine DC Parameters of Solar Cells : A Critical Review," Renewable and Sustainable Energy Reviews, no. 28, pp. 588-596, 2013.

[17] C. Linear Technology, "LT Spice IV," http://www.linear.com/designtools/software/#LTspice, 2015.

[18] N. Grossiord, J. M. Kroon, R. Andriessen, and P. W. M. Blom, "Degradation mechanisms in organic photovoltaic devices," Organic Electronics, vol. 13, no. 3, pp. 432-456, Mar, 2012.

[19] C. J. Schaffer, C. M. Palumbiny, M. A. Niedermeier, C. Jendrzejewski, G. Santoro, S. V. Roth, and P. Muller-Buschbaum, "A direct evidence of morphological degradation on a nanometer scale in polymer solar cells," Advanced Materials, vol. 25, pp. 6760-6764, 2013.

Krisna Adhitya received an MSc. degree in Nanoscale Science and Technology from The University of Sheffield, Sheffield, UK in 2009.

He is currently working towards the Ph.D degree in physics with The University of Sheffield, UK. His current research interest includes intensity-modulated spectroscopy, impedance spectroscopy and organic photovoltaic cells.

Abdullah Alsulami received the BSc. in physics and an MSc. degree in laser physics from King Saud University, Riyadh, Saudi Arabia.

He is currently working towards the Ph.D degree in physics with The University of Sheffield, UK. His current research interest includes impact of interfaces between different hole transport thin films and active layer in organic solar cells performances.

Alastair Buckley received the Ph.D degree in chemistry from The University of Sheffield, Sheffield, UK. He currently holds a lectureship in Organic Electronics and Photonics in The University of Sheffield, UK.

His research interest is themed around understanding and applying the intrinsic advantages of functional organic materials to a wide range of optoelectronic devices.

Richard C. Tozer (M'83-SM'98) received the B.Eng. and Ph.D. degrees from the University of Sheffield, Sheffield, U.K., in 1970 and 1975, respectively. Following a period of postdoctoral research at the University of Sheffield in the area of CCD applications, he became a Lecturer in active sound cancellation at the University of Essex, Colchester, U.K. In 1980, he returned to the University of Sheffield as a Lecturer, where he now teaches analog circuit design.

His research activities involve the application of analog circuits to a wide range of experimental and instrumentation problems and is currently centered around avalanche photodiode noise measurement and novel excitation modes for fluorescent lamps. Professor. Tozer is a Chartered Engineer and a Member of the Institute of Electrical Engineers (IEE).

Martin Grell is a senior lecturer in the Department of Physics and Astronomy at the University of Sheffield, UK. He received his 'Dr. rer. nat.' degree from the Technical University, Darmstadt, Germany in 1994 for his work on polymer physics under the supervision of Prof. J H Wendorff. He was then awarded a Marie Curie postdoctoral fellowship for research on bioploymers at the University of Wales, Bangor, UK, and in 1996 joined Prof DDC Bradley's organic semiconductor research group as a postdoc. In 2000, he was appointed lecturer at Sheffield University. His research was in the physics and physical chemistry of organic semiconductors and development of photonic and electronic devices, in particular, thin film field effect transistors.

In recent years, he has developed innovative thin film sensor devices, and electrolyte-gated thin film transistors, including real-time electronic read-out schemes for such devices.

Supplementary information

Organic Solar Cell Preparation and Characterisation

We here studied a state-of-the-art BHJ OPV cells using as its active layer a blend of a low bandgap hole transporting semiconducting polymer, abbreviated PFDT2BT-8 (inset to Fig. S1), and an electron accepting C_{70} derivative, with a PEDOT:PSS hole extracting layer. Cells were prepared in groups of 6 pixels on a single device substrate. PEDOT:PSS was purchased from Ossila Ltd, whilst PFDT2BT-8 was synthesized in the Department of Chemistry at the University of Sheffield via a previously reported method [15], and had a molecular weight of of 91.6 KDa and a PDI of 1.47 [15]. $PC_{70}BM$ was purchased from Ossila Ltd with a purity of 95% (5% $PC_{60}BM$). The active layer solution was prepared by mixing PFDT2BT-8 and $PC_{70}BM$ at a weight ratio of 1:4 in chloroform with an overall concentration of 20 mg.ml^{-1}. Subsequently, the solutions were placed onto a hotplate at 55 °C for a few hours before they were filtered through a 0.45-μm PTFE filter. All devices were fabricated onto 15 x 20 mm^2 of pixellated cathode design glass substrates that were supplied by Ossila. These substrates are sold pre-patterned with a 100 nm layer of Indium Tin Oxide (ITO). Prior to use, the substrates were sonicated in a warm cleaning solution of either NaOH (10 wt% in water) or Hellmanex (2 wt%) for 10 minutes and then deionised in water for 5 minutes followed by warm IPA for 5 minutes. Finally, they were dried with nitrogen gas. PEDOT:PSS film with (30 nm ± 3 nm) thickness was spin cast in ambient conditions and then was annealed at 130 °C for 30 minutes in glove box environment. The active semiconductor layer was prepared by spin casting the solution onto a substrate at a spin speed of 3000 rpm in order to obtain an active film with a thickness of 70 nm ± 3 nm. The bi-layer cathodes of Ca (5nm) and Al (100 nm) were evaporated at a rate of 3 Å.s^{-1} and 10 Å.s^{-1}. Finally, the central area of each substrate was encapsulated by using a glass slide and light-curable epoxy. For DC j(V) characterisation (but not for IMS), device pixels were covered by a 2.6 mm^2 shadow mask and were characterised under ambient conditions using a Keithley 2400 source meter and a Newport 92251A-1000 AM 1.5 solar simulator. An NREL calibrated silicon diode was used to calibrate the power output at 100 mW.cm^{-2}. The j/V characteristic of a device pixel under AM 1.5 is shown in Fig. S1. Despite best attempts to achieve identical processing conditions for each device, not all pixels performed to that standard. The box plot Fig. S2 illustrates performance statistics for 54 pixels (9 device substrates x 6 pixels each). Most pixels were 'good' with very similar PCE (~ 6%), but a few 'bad' pixels fall short to different extends. We have chosen a representative 'good' pixel for IMS.
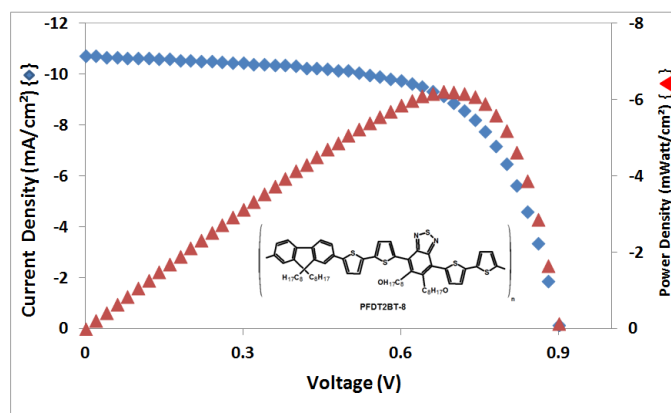

Fig. S1. j/V characteristics of the OPV cell used here and the power profile AM 1.5 illumination.

Fig. S1 gives us j_{SC} = -10.7 mAcm^{-2}, V_{OC} = 902 mV, V_{MPP} = 680 mV, and maximum power density 6.2 mWcm^{-2}. From the j/V characteristic, specific serial resistance R_s = 12.6 Ωcm^2 and specific shunt resistance R_{sh} = 1820 Ωcm^2 can be derived [16]; for an active device area of 2.6 mm^2 that translates into R_{Sh} = 70 kΩ, and R_S = 520 Ω.
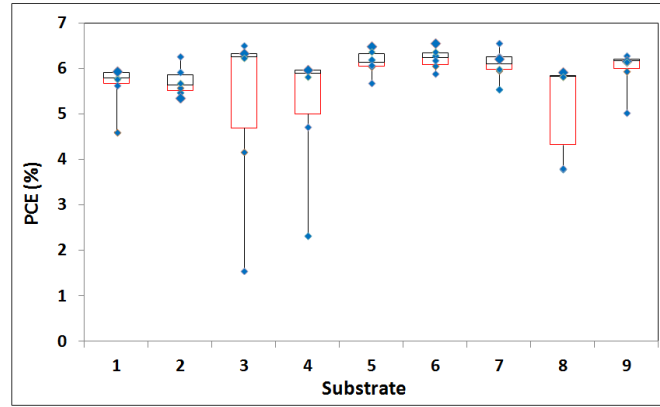
Fig. S2: Box plots illustrating the performance statistics of pixels on different device substrates. Power conversion efficiency (PCE, blue circles) is about 6% for all 'good' pixels.

Tabulated Characteristics of IMS Spectra, Fig. 3

Table S1 summarises the electric conditions (loads R_L and DC voltage points, i.e. the voltages selected by the respective R_L, as well as the corresponding current densities j, under LED illumination), and characteristic parameters f_c, *Re ΔV (f → 0))* extracted from the IMS spectra shown in Fig. 4.

TABLE S1
LOAD R_L, RESULTING VOLTAGE POINTS AND CURRENT DENSITIES, CORNER FREQUENCIES f_c, AND *Re ΔV* FOR f → 0, FOR
THE SPECTRA SHOWN IN FIG. 3

R_L [kΩ]	Voltage point [mV]	R1/3 j [mA/cm^2]	f_C [Hz]	*Re ΔV (f→0)* [mV]
6.8	100	0.51	3208	17
13.4	200	0.52	1724	33
19.9	300	0.53	1404	46
26.5	383	0.51	1030	57
27.7	400	0.50	1029	60
34.4	480	0.49	837	68
36.6	505	0.48	753	70
47.6	603	0.44	836	70
54.8	650	0.41	927	62
61.8	683	0.39	1140	53
66.7	700	0.37	1140	46
95.4	750	0.27	2121	25
158	780	0.17	3208	15
476	800	0.06	13666	10

The current density (j) column is calculated from the chosen R_L and resulting voltage point, V, as j = R_L / (V*A), A = device area = 2.86 mm^2. Columns f_c and *Re ΔV (f → 0)* were used to construct Fig. 4. Column j is used to construct Fig. S2, the j(V) characteristic under red LED illumination

Current/voltage Characteristics under LED Illumination

Solar cell characteristics, and also the extracted equivalent circuit parameters, depend on the intensity of illumination. For IMS, we illuminated our cells with a red LED driven by (18 ± 4) mA, which is much less intense than AM 1.5. We have therefore

constructed an alternative DC j(V) characteristic to Fig. S.1 from the j(V) data from table S1, which corresponds to red LED illumination. The result is shown in Fig. S4. From Fig. S3 we find j_{sc} = -0.51 mAcm^{-2}, V_{OC} = 800 mV, V_{MPP} = 650 mV, and P_{MPP} = 270 μWcm^{-2} . From the LED j/V characteristics, we find also the OPV's specific R_{sh} = 10000 Ωcm^2 and its specific R_s = 182 Ωcm^2, using the same derivation method [16] as in Fig. S1. This equates to R_{sh} = 350 kΩ and R_s = 6.4 kΩ. However, due to the lower quality of the j(V) characteristics under red LED, the latter parameters in particular are difficult to extract accurately.
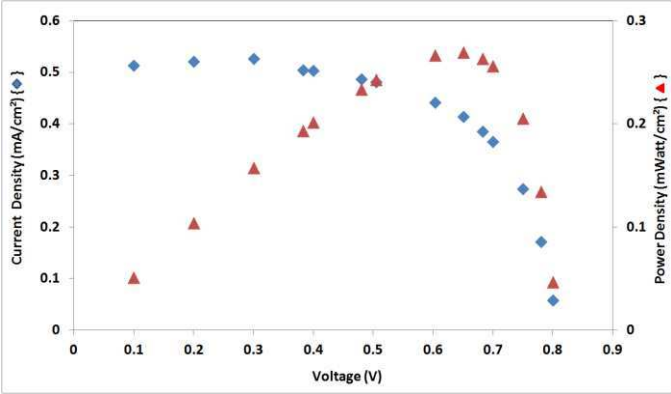

Fig. S4: j(V) characteristics and power profile under red LED illumination, constructed from table S1.
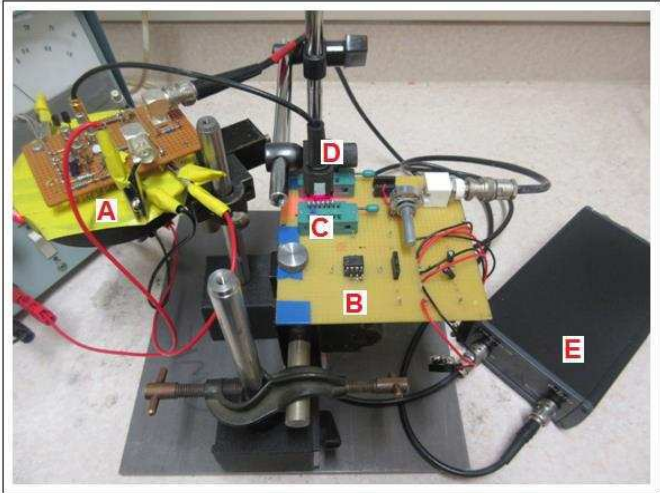
Photograph of Our Set Up

Fig. S5: Photograph of our set-up. A is the bespoke voltage adder circuit, B is the OPV testing module, C is the OPV under characterization, D is the red LED (650 nm) used here and E is the USB-based lock-in amplifier that generates its own sinusoidal reference voltage. The Lock-In was linked to a PC (not shown here) via USB cable. Reference frequency was set, and data were collected, on the PC using LabView software.